

## AGN jet-inflated bubbles as possible origin of odd radio circles

YEN-HSING LIN <sup>1</sup> AND H.-Y. KAREN YANG <sup>1,2</sup>

<sup>1</sup>*Institute of Astronomy, National Tsing Hua University, Hsinchu 30013, Taiwan*

<sup>2</sup>*Physics Division, National Center for Theoretical Sciences, Taipei 106017, Taiwan*

### ABSTRACT

Odd radio circles (ORCs) are newly discovered extragalactic radio objects with unknown origin. In this work, we carry out three-dimensional cosmic-ray (CR) magnetohydrodynamic simulations using the FLASH code and predict the radio morphology of end-on active galactic nucleus (AGN) jet-inflated bubbles considering hadronic emission. We find that powerful and long-duration CR proton (CRp)-dominated jets can create bubbles with similar sizes ( $\sim 300 - 600$  kpc) and radio morphology (circular and edge-brightened) to the observed ORCs in low-mass ( $M_{\text{vir}} \sim 8 \times 10^{12} - 8 \times 10^{13} M_{\odot}$ ) halos. Given the same amount of input jet energy, longer-duration (thus lower-power) jets tend to create larger bubbles since high-power jets generate strong shocks that carry away a significant portion of the jet energy. The edge-brightened feature of the observed ORCs is naturally reproduced due to efficient hadronic collisions at the interface between the bubbles and the ambient medium. We further discuss the radio luminosity, X-ray detectability, and the possible origin of such strong AGN jets in the context of galaxy evolution. We conclude that end-on CR-dominated AGN bubbles could be a plausible scenario for the formation of ORCs.

*Keywords:* cosmic rays – galaxies: active – galaxies: clusters: intracluster medium – hydrodynamics – methods: numerical

### 1. INTRODUCTION

Odd radio circles (ORCs) are extragalactic, edge-brightened, circular, low surface brightness radio objects that have no obvious counterpart emission in the optical, near-infrared (NIR), and X-ray bands. They are discovered in 2021 by Norris et al. (2021a) in ASKAP EMU Pilot survey (Norris et al. 2021b) and GMRT, with subsequent discovery published by Koribalski et al. (2021, 2023) and Gupta et al. (2022). Optical/NIR spectroscopic follow-up observations of their suspected host galaxies have also been presented (Coil et al. 2023; Rupke et al. 2023). After their discovery, several possible scenarios about their origin have been proposed, including structure formation shocks (Yamasaki et al. 2023), galaxy mergers (Dolag et al. 2023), or, in con-

trast to the argument of Norris et al. (2021a), supernova remnants (e.g. Sarbadhicary et al. 2023).

Norris et al. (2022) investigated one of the ORCs (ORC1) using the MeerKAT telescope (Jonas & MeerKAT Team 2016) and measured the spectral index and polarization with high angular resolution. They discussed three possible formation scenarios of the ORCs, including shocks from explosive events in the host galaxy, star formation termination shocks, and end-on radio bubbles generated by active galactic nucleus (AGN) jets. In the last scenario, relativistic jets from the central AGN would propagate into the intracluster/intragroup medium (ICM/IGM) and create low density regions (often referred to as radio bubbles or AGN bubbles) that are filled with cosmic rays (CRs) (e.g., Dunn & Fabian 2004). The CRs within the bubbles could emit synchrotron radiation that lasts longer than the jet duration, depending on the cooling times of the CRs. If the system is viewed side-on (that is, if the jet axis is perpendicular to the line of sight), it would be classified as typical radio bubbles. On the other hand, if the jet axis is nearly parallel to the line of sight, the

Corresponding author: Yen-Hsing Lin  
julius52700@gmail.com

hyang@phys.nthu.edu.tw

radio-emitting bubbles could overlap with each other, forming a circular radio object that might be classified as an ORC.

Nevertheless, previous AGN jet simulations (see e.g. Blandford et al. 2019; Bourne & Yang 2023, for recent reviews) rarely produce radio lobes or bubbles that are sufficiently large to explain the ORCs. For instance, in the simulations of Lin et al. (2023), the jets with power of  $5 \times 10^{45} \text{ erg s}^{-1}$  and duration of 10 Myr could only create bubbles with a radius of  $\sim 20 \text{ kpc}$  in a Perseus-like cluster environment (a cool-core cluster with virial mass  $M_{\text{vir}} \sim 8 \times 10^{14} M_{\odot}$ ), which is an order of magnitude smaller than what is required to explain the ORCs. There are potentially several ways to enlarge the size of the bubbles. After injection, the bubbles would gradually expand and approach pressure equilibrium with the ambient medium. Therefore, the size of the bubbles depends on the total energy stored within them and the ambient gas pressure profiles. The simplest way to expand the bubbles is thus increasing the power and duration of AGN jets. Another way is to decrease the mass of the system, so that the bubbles could expand more easily due to the lower pressure and weaker gravitational potential.

In this work, we aim to demonstrate that, under suitable parameter combinations, end-on AGN jet-inflated bubbles can reproduce properties of the observed ORCs. We organize the structure of this paper as follows. In Section 2, we describe the simulation setup and the treatment of CR transport and heating/cooling processes. In Section 3, we describe the dynamics and expected radio morphology of the simulated bubbles. In Section 4, we discuss the absolute brightness of the simulated ORCs, the possible origin of the strong jets in the context of galaxy evolution, and the caveats that should be addressed in future investigations. We summarize our conclusions in Section 5.

## 2. METHODS

We perform three-dimensional (3D) CR-magnetohydrodynamic (CR-MHD) simulations of AGN jets in a self-similar cluster environment using the adaptive mesh refinement (AMR) FLASH code (Fryxell et al. 2000). The simulation setup and cluster environment are described in Section 2.1 and Section 2.2, respectively. We then produce simulated radio images by calculating synchrotron emissivity of the grid cells and integrating them along any given line of sight using methods described in Section 2.3.

### 2.1. CR-MHD simulations

In this work, we model the evolution of AGN jet-inflated bubbles by injecting mass, momentum, and en-

ergy of bipolar jets from a cylinder located at the center of the simulation domain, following prescriptions of Yang et al. (2019) (see also Yang et al. (2012)). We assume the AGN jets are dominated by CR protons (CRp), identical to the CRpS simulation performed by Lin et al. (2023) (S here represents the inclusion of CR streaming). As will be discussed in Section 3, choosing CRp dominated jets is key for reproducing the observed features of ORCs. The simulation box size is set to 1 Mpc in order to simulate bubbles with a diameter over 500 kpc (similar to ORC1). The simulation time is set to 200 Myr.

Since the bubbles occupy a significant portion of the simulation box, and it would be too computationally expensive to refine the whole bubbles to maximum resolution using standard AMR criteria, we adopt the following strategy to determine the refinement levels within the simulation domain. Specifically, we set the maximum refinement level to 9 within the central 20 kpc in order to properly resolve the jet launching region (with a maximum spatial resolution of 0.5 kpc). Regions located more than 20 kpc away from the center are assigned a maximum refinement level of 6, corresponding to a spatial resolution of 4 kpc. This approach significantly reduces the computational cost while still capturing the large-scale evolution of the bubbles. By performing convergence tests with different outskirts refinement levels, we verified that the simulated bubble size is robust.

We adopt the CR-MHD formalism (Zweibel 2013, 2017) to model the interaction between the injected CRs and thermal gas in the cluster. To first order, the CRs are coupled with the thermal gas because CRs are well scattered by tangled magnetic field. Therefore, on macroscopic scales (much greater than the CR gyro radii), one can treat CRs as a second fluid and solve the following CR-MHD equations:

$$\frac{\partial \rho}{\partial t} + \nabla \cdot (\rho \mathbf{v}) = 0 \quad (1)$$

$$\frac{\partial \rho \mathbf{v}}{\partial t} + \nabla \cdot \left( \rho \mathbf{v} \mathbf{v} - \frac{\mathbf{B} \mathbf{B}}{4\pi} \right) + \nabla p_{\text{tot}} = \rho \mathbf{g} \quad (2)$$

$$\frac{\partial \mathbf{B}}{\partial t} - \nabla \times (\mathbf{v} \times \mathbf{B}) = 0 \quad (3)$$

$$\begin{aligned} \frac{\partial e}{\partial t} + \nabla \cdot \left[ (e + p_{\text{tot}}) \mathbf{v} - \frac{\mathbf{B}(\mathbf{B} \cdot \mathbf{v})}{4\pi} \right] \\ = \rho \mathbf{v} \cdot \mathbf{g} + \nabla \cdot (\boldsymbol{\kappa} \cdot \nabla e_{\text{cr}}) + \mathcal{H}_{\text{cr}} - n_e^2 \Lambda(T) \end{aligned} \quad (4)$$

$$\frac{\partial e_{\text{cr}}}{\partial t} + \nabla \cdot (e_{\text{cr}} \mathbf{v}) = -p_{\text{cr}} \nabla \cdot \mathbf{v} + \nabla \cdot (\boldsymbol{\kappa} \cdot \nabla e_{\text{cr}}) + \mathcal{C}_{\text{cr}} \quad (5)$$

Parameter	Symbol	Value
Virial Mass	$M_{\text{vir}}$	$8 \times 10^{14} M_{\odot}$
Virial Radius	$R_{\text{vir}}$	2440 kpc
Baryon fraction	$M_g/M_{\text{vir}}$	0.15
Central temperature	$T_c$	7 keV
Concentration	$c$	6.81
Magnetic field	$b_{\text{norm}}$	0.01
Jet power	$P_0$	$5 \times 10^{45} \text{ erg s}^{-1}$
Jet duration	$D_0$	10 Myr

**Table 1.** Fiducial parameters for our cluster setup.

where  $\rho$  and  $\mathbf{v}$  are the gas density and velocity, respectively,  $\mathbf{g}$  is the gravitational field, and  $\kappa$  is the CR diffusion tensor, which describes the second-order effect of CR transport.  $e_{\text{cr}}$  is the CR energy density and  $e$  is the total energy density, consisting of kinetic, thermal, CR and magnetic energy ( $e = 0.5\rho v^2 + e_{\text{th}} + e_{\text{cr}} + B^2/8\pi$ ). The total pressure is  $p_{\text{tot}} = (\gamma - 1)e_{\text{th}} + (\gamma_{\text{cr}} - 1)e_{\text{cr}} + B^2/8\pi$ , in which we adopt the adiabatic index  $\gamma = 5/3$  for the thermal gas and  $\gamma_{\text{cr}} = 4/3$  for relativistic CRs.  $\mathcal{H}_{\text{cr}}$  is the net contribution of CR related processes to the change of total energy density,  $\mathcal{C}_{\text{cr}}$  is the CR cooling rate due to the combined effect of Coulomb losses, hadronic processes, and CR streaming. Inverse-Compton (IC) scattering and synchrotron losses are neglected in the simulations because the jets are assumed to be CRp dominated.  $n_e$  is the electron number density, and  $\Lambda(T)$  is the radiative cooling function. We refer the readers to Lin et al. (2023) for additional details.

### 2.2. Setup of the cluster environment

We assume that the gas in the cluster follows the same temperature profile as the observed Perseus cluster and is initially in hydrostatic equilibrium within a static gravitational potential described by the NFW profile (Navarro et al. 1995). The system is characterized by the virial mass ( $M_{\text{vir}}$ ), virial radius ( $R_{\text{vir}}$ ), central temperature ( $T_c$ ), concentration parameter ( $c$ ) and baryon fraction ( $M_g/M_{\text{vir}}$ ). As mentioned in Section 1, bubbles only grow to  $r \sim 20$  kpc in a high mass ( $M \sim 8 \times 10^{14} M_{\odot}$ ) cluster. In order to reproduce the observed ORCs, a smaller ambient pressure, and thus a less massive cluster is required. To this end, we set up the gas profiles using the self-similar scaling relations of galaxy clusters (Kaiser 1986; Yang & Reynolds 2016):

$$R_{\text{vir}} \propto M_{\text{vir}}^{1/3}, \quad T_c \propto M_{\text{vir}}^{2/3}, \quad c \propto M_{\text{vir}}^{-0.08}. \quad (6)$$

A tangled magnetic field is generated by performing 3D inverse Fourier transform of a magnetic power spectrum with a coherence length of 100 kpc (see e.g. Yang & Ruszkowski 2017, for detailed descriptions). To fix the

plasma beta parameter  $\beta = P_{\text{th}}/P_B$ , we normalize the magnetic field strength with a parameter  $b_{\text{norm}} \propto M_{\text{vir}}^{2/3}$  to keep a constant value of  $\beta \sim 100$  (Carilli & Taylor 2002; Feretti et al. 2012). The fiducial parameters are summarized in Table 1.

For the following discussion, we employ the naming convention [Physics]\_M[Mass]\_P[Power]\_D[Duration]. For instance, the simulation denoted as CRpS\_M12\_P5\_D5 represents the simulation that uses CRpS jets in a cluster with virial mass  $M_{\text{vir}} = 8 \times 10^{12} M_{\odot}$ , jet power of five times the fiducial value ( $2.5 \times 10^{46} \text{ erg s}^{-1}$ ), and jets that last for five times the fiducial duration (50 Myr).

### 2.3. Radio signatures

In the hadronic scenario considered in this study, the radio emission comes from synchrotron radiation of secondary electrons and positrons produced by the hadronic collisions between the injected CRp and the ambient medium (e.g., Owen & Yang 2022). While it is possible to calculate the synchrotron emissivity (using methods described in Appendix C in Lin et al. 2023), solving for the distributions of secondary particles across the whole simulation box is computationally expensive and unnecessary for the purpose of simple morphological comparison. Also, to compute the absolute values of the synchrotron emissivity involves a number of uncertainties (see discussion in Section 4.2). Therefore, for the content presented in this paper, we adopt a simplified method that assumes the radio emissivity of a given cell to be proportional to the hadronic cooling rate of CRp (which approximates the secondary-particle production rate under the steady-state assumption) and the strength of the magnetic field squared ( $\epsilon \propto \mathcal{C}_{\text{CRp,h}} \propto e_{\text{cr}}\rho B^2$ , Yoast-Hull et al. 2013; Ruszkowski et al. 2017). After calculating the emissivity of each grid cell, we then perform integration along a given axis and obtain a predicted radio image.

To allow direct comparison to the observed ORCs, we convolve the radio image with a Gaussian kernel that has a standard deviation ( $\sigma$ ) corresponding to a 6-arcsecond beam size (Norris et al. 2022). The conversion of the kernel size between the angular size (in units of arcseconds) and physical size (in units of pixels on the image) is done by considering the angular diameter distance ( $d_A(z)$ ) in a flat LambdaCDM cosmology with  $\Omega_{\text{m},0} = 0.3$  and  $h_0 = 0.7$ , i.e.,

$$\sigma(\text{pixel}) = 25.67 \left( \frac{d_A(z)}{1324 \text{ Mpc}} \right) \left( \frac{\text{Beam size}}{6 \text{ arcsecond}} \right) \times \left( \frac{\text{Image size}}{800 \text{ pixel}} \right) \left( \frac{\text{Box size}}{1200 \text{ kpc}} \right), \quad (7)$$

where  $d_A(z)$  depends on the redshift ( $z$ ) of the ORC of interest and is calculated using the `astropy.cosmology` Python module (Astropy Collaboration et al. 2022).

### 3. RESULTS

#### 3.1. Benchmark cases

In this section, we describe two of the most promising simulations, namely CRpS\_M12\_P5\_D5 and CRpS\_M13\_P5\_D5 in detail.

The top panel of Fig. 1 displays the simulated radio image of CRpS\_M12\_P5\_D5 (left) at 200 Myr with a viewing angle of  $0^\circ$  (line of sight parallel to the jet axis) and the observed image of ORC1 (right), linearly normalized with the maximum value in the image. Both images have a side length of roughly 1200 kpc. From the images, it is evident that end-on AGN jet-inflated bubbles can indeed produce a circular radio object with a diameter comparable to ORC1 (520 kpc, Norris et al. 2022). The edge-brightened feature is also reproduced with reasonable contrast between the edge and the interior of the object. Consistencies can also be found in the comparison between CRpS\_M13\_P5\_D5 and ORC5 (bottom panel of Fig. 1; each image has a side length of 600 kpc). Note that due to the deeper gravitational potential well and higher ambient gas pressure, the bubble radius in CRpS\_M13\_P5\_D5 is roughly two times smaller than that in CRpS\_M12\_P5\_D5, despite the same jet power and duration. Furthermore, because of the large difference in bubble volume, the surface brightness of CRpS\_M12\_P5\_D5 is roughly 1000 times fainter than CRpS\_M13\_P5\_D5 since its CR energy density ( $e_{\text{cr}}$ ), gas density ( $\rho$ ), and magnetic field strength ( $B$ ) are all smaller in the lower mass system.

The key mechanism that enables us to reproduce the limb-brightened feature lies in the nature of the hadronic processes. As mentioned in Section 2.3, the synchrotron emissivity is directly proportional to  $e_{\text{cr}}$  and  $\rho$ . Although  $e_{\text{cr}}$  is high within the bubbles, hadronic collisions are inefficient due to the low gas density. Conversely, the ambient ICM exhibits a relatively high gas density but lacks CRs for interaction. The confluence of high  $e_{\text{cr}}$  and  $\rho$  occurs only at the interface between the bubbles and ICM. A schematic diagram illustrating this idea is shown in Fig. 2.

One drawback of the AGN scenario, as discussed in Norris et al. (2022), is the requirement of a highly aligned jet axis with the line of sight, which seems coincidental. To investigate the dependence of ORC properties on the viewing angle, we present the radio maps of both CRpS\_M12\_P5\_D5 and CRpS\_M13\_P5\_D5 at 200 Myr with viewing angles ranging from  $0^\circ$  to  $90^\circ$  in Fig. 3. It is evident that the eccentricity of the rings remains

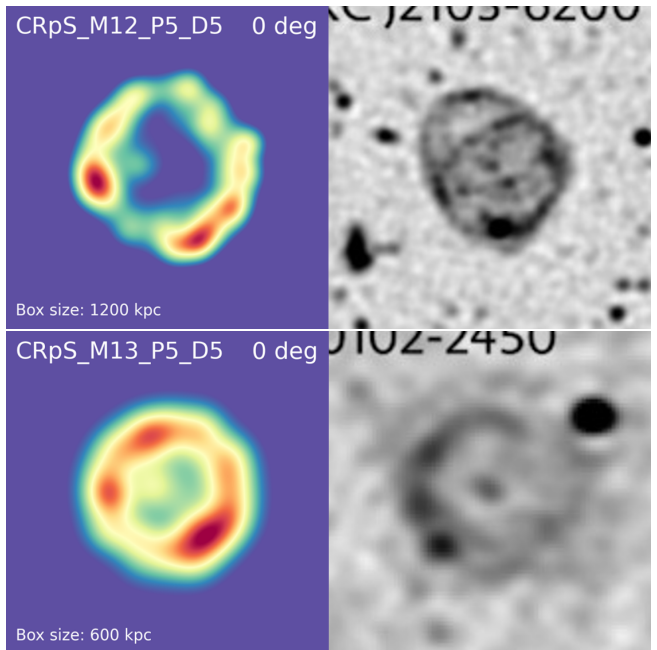


**Figure 1.** *Top panel:* Comparison between the simulated radio image in CRpS\_M12\_P5\_D5 at 200 Myr (left) and the observed ORC1 (right). *Bottom panel:* Comparison between the images of CRpS\_M12\_P5\_D5 at 200 Myr and ORC5. Images of ORC1 and ORC5 are retrieved from Norris et al. (2022) and cut to approximately the same physical size as the simulated ones. The simulated images are obtained by assuming a viewing angle aligned with the jet axis and are smoothed by assuming that they are located at  $z = 0.551$  (same as ORC1) and  $z = 0.27$  (same as ORC5), respectively. The colorscale is linearly normalized to the maximum brightness in each image.

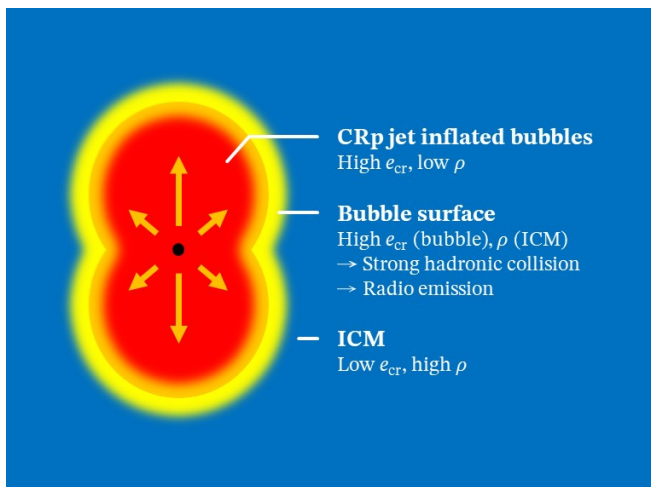


**Figure 2.** Schematic diagram that illustrate the key idea of the hadronic AGN bubble scenario. By combining the high gas density in the ambient ICM and high CRp energy density within the bubbles, the surface of the bubbles can naturally reproduce the edge-brightened feature of the observed ORCs after projected along the jet axis.

consistent with ORC1 up to an angle of  $\sim 30^\circ$  between the jet axis and the line of sight. The shape of the ring is relatively insensitive to the viewing angle because CR dominated jets tend to generate round bubbles (rather than elongated bubbles inflated by kinetic-energy dominated jets; Yang et al. 2019). Although predicting the probabilities of observing the ORCs and their number densities requires further investigation, our results suggest that the issue of viewing-angle alignment may not be as severe as one may naively expect.

It is also worth noting that the emission of the simulated bubbles is not smoothly distributed at the interface between the bubbles and the ICM. Instead, a significant portion of the emission originates from numerous small, luminous clumps scattered across the surface of the bubbles, which are formed due to local fluid and thermal instabilities. As the gas cools and condenses into these dense clumps, not only does the hadronic collision rate increase, but the magnetic field strength is also enhanced due to flux freezing. The ring-like structure in Fig. 1 actually consists of multiple small and bright synchrotron-emitting clumps rather than a single, smooth surface. Therefore, as the viewing angle increases, the system would become very clumpy and may not be classified as an ORC observationally (e.g. CRpS\_M12\_P5\_D5 with  $90^\circ$  viewing angle in Fig. 3). Moreover, our results imply that with higher resolution observations (e.g. VLA or SKA), one should be able to resolve the rings into many small and bright clumps. This feature could serve as one prediction of our model.

### 3.2. Parameter search

To explore the parameter dependence of the simulated ORCs, we carry out a series of simulations to investigate how the jet power, jet duration, and cluster mass affect the dynamics and radio morphology of the bubbles. Fig. 4 shows the side-on time series of density slices of simulations with different parameter combinations. The top three rows show the results for a virial mass  $M_{\text{vir}} = 8 \times 10^{13} M_\odot$ , and the bottom three rows are for  $M_{\text{vir}} = 8 \times 10^{12} M_\odot$ . Among the simulations with the same cluster mass, the first row represents a simulation with the fiducial jet power ( $P_0$ ) but a long jet duration ( $5D_0$ ). The second row shows the results for a high jet power ( $5P_0$ ) and the fiducial jet duration ( $D_0$ ). The simulation shown in the third row, as described in Section 3.1, features both a high jet power ( $5P_0$ ) and a high jet duration ( $5D_0$ ). In Fig. 5 and 6, we show the intrinsic and smoothed end-on radio images of the corresponding simulations, respectively. Several points can be drawn from the figures:

1. Given the same total input energy, systems with a higher jet power tend to produce bubbles with a smaller volume. This is because more powerful jets would generate stronger shocks that carry energy away and reduce the amount of energy stored within the bubbles to drive bubble expansion. This is consistent with previous findings by Tang & Churazov (2017).
2. If the total input energy is insufficient, the ICM would efficiently cool via radiative cooling and collapse back onto the bubbles, as seen in the first and second rows in Fig. 4. By contrast, in the low mass ( $M_{\text{vir}} = 8 \times 10^{12} M_\odot$ ) system, the same jets can evacuate the ambient medium from the central region more effectively.
3. As mentioned in Section 3, the radio emission in our simulations mainly comes from small and bright clumps formed via hydrodynamic and thermal instabilities near the bubble surface. Therefore, the beam size of the observation would have a great impact on the morphology of the objects. For instance, with a 6-arcsecond beam, CRpS\_M13\_P5\_D5 and CRpS\_M12\_P1\_D5 exhibit very similar radio morphology (Fig. 6). However, their intrinsic morphology (e.g. the number of bright clumps and brightness contrast between their edges and interiors) are significantly different (Fig. 5). The underlying physical properties of the two systems (cluster mass and jet power) are also substantially different.

## 4. DISCUSSION

### 4.1. Requirements for reproducing the ORCs

In this section, we discuss several lessons learned for creating ORC-like objects using CRp dominated AGN bubbles.

First of all, in order to produce bubbles with radii comparable to the observed ORCs, the power and duration of the jets must be strong enough to completely evacuate the high density gas originally sitting near the center of the cluster. If this is not achieved, the central high density gas would easily dominate the synchrotron emission ( $\epsilon \propto e_{\text{cr}} \rho B^2$ ) and create a centrally brightened radio source. Note that even if the ICM is temporarily evacuated, gas could still cool (especially if compressed) through radiative cooling and eventually fall back toward the central region. Therefore, the total energy input from the AGN jets should be significantly larger than the gravitational potential energy of the inner ICM/IGM.

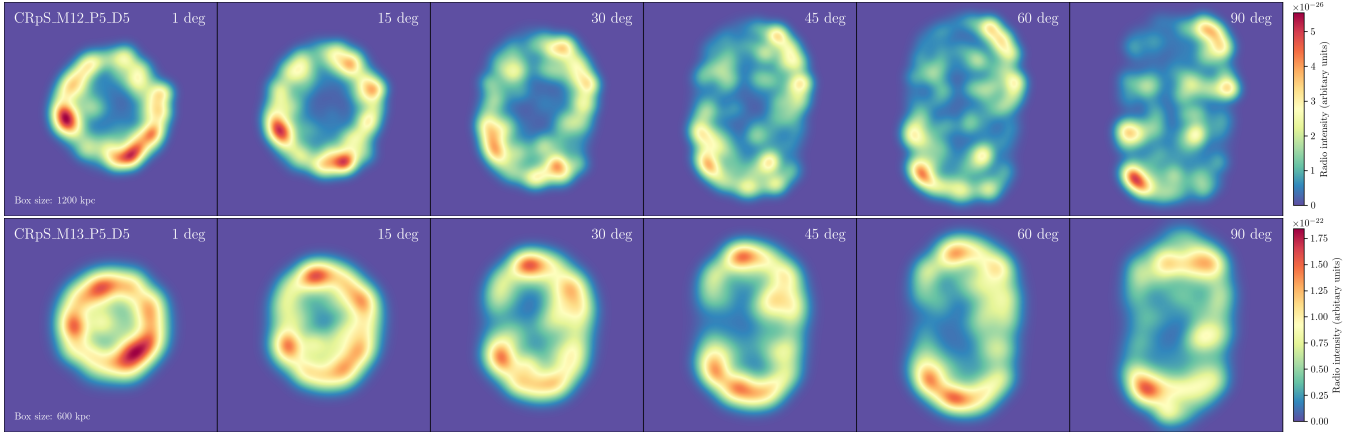


**Figure 3.** Simulated radio images of CRpS\_M12.P5.D5 and CRpS\_M13.P5.D5 at 200 Myr with viewing angles ranging from  $0^\circ$  to  $90^\circ$  with respect to the jet axis. The box sizes are 1200 kpc (top row) and 600 kpc (bottom row), respectively. While the absolute value of the colorbar is arbitrary, the relative value between the two simulations does carry physical meanings – the ORC in CRpS\_M12.P5.D5 is significantly fainter than that in CRpS\_M13.P5.D5 (see discussion in Section 3.1).

CRpS jets could naturally reproduce the edge-brightened morphology of the observed ORCs because the hadronic collision is most efficient at the interface between the bubbles and the ICM (Fig 2). On the other hand, if the jets are CRe dominated (Dunn & Fabian 2004; Bîrzan et al. 2008; Croston et al. 2018; Lin et al. 2023), the synchrotron emissivity is instead  $\epsilon \propto e_{\text{cr}} B^2$ . In this case, one would generally produce a centrally brightened radio object instead of an edge-brightened one, because the synchrotron emissivity is largely uniform in the bubble interior, and the pathlength is the greatest along the jet axis. The edge-brightened feature could be produced in some cases if the magnetic field strength is enhanced by adiabatic compression at the interface between the bubbles and the ICM, where the compression could occur due to bubble expansion and fallback of the ICM in response to radiative cooling. However, this feature is short-lived and requires fine-tuning of the parameters. Most important of all, given the old age (200 Myr) of the bubbles, the primary CRe injected by the AGNs should have cooled below the energy required to shine at the observed frequency. For instance, in Norris et al. (2022), ORC1 ( $z = 0.551$ ) is observed with MeerKAT at around 1 GHz, we can therefore estimate the corresponding CRe energy to be:

$$E_{\text{CRe}}(\nu_{\text{obs}}) = \gamma m_e c^2 \sim \sqrt{\frac{(1+z)\nu_{\text{obs}}}{\nu_G}} m_e c^2, \quad (8)$$

where  $\gamma$  is the Lorentz factor of the CRe, and the gyro frequency  $\nu_G$  can be obtained by the relation

$$\frac{\nu_G}{\text{MHz}} = 2.8 \times \frac{B}{\text{Gauss}}. \quad (9)$$

Assuming  $B = 0.1 \mu\text{G}$ , the corresponding CRe energy is  $E_{\text{CRe}}(1 \text{ GHz}) \sim 40 \text{ GeV}$ . Because the magnetic field

strength is small, CRe cooling is dominated by IC scattering of the cosmic microwave background (CMB) photons. We can then estimate the CRe cooling time as

$$\tau_{\text{IC}} \sim 3 \times 10^7 \text{ sec} \frac{1}{\gamma u_{\text{rad}}}, \quad (10)$$

where  $u_{\text{rad}} = 4.2 \times 10^{-13} (1+z)^4 \text{ erg cm}^{-3}$  is the energy density of the CMB radiation field. For  $z = 0.551$  and  $\gamma = E_{\text{CRe}}/(m_e c^2) \sim 7.83 \times 10^4$ , the CRe cooling time is  $\sim 5 \text{ Myr}$ , significantly shorter than the formation time of the bubbles. It is therefore evident that given the bubble age of 200 Myr, the primary CRe from AGN jets would have cooled below the observable frequency, necessitating shock/turbulence reacceleration in the leptonic scenario.

#### 4.2. Remarks on the absolute brightness

While our setup could successfully reproduce the size and morphology (that is, relative brightness) of the ORCs, it is important to ask whether the specific intensity produced by our simulated ORCs are comparable to the observed ones.

However, there are several factors that can cause large uncertainties in the calculations of the absolute brightness in our model. First of all, since the radio emission mainly comes from high density clumps originating from hydrodynamic instabilities and radiative cooling, the predicted intensity of the ORCs is very sensitive to how large the cold clumps are, which is typically non-convergent in numerical simulations. The dependence of observed intensity on clump size can be understood as follows. Consider a region on the bubble surface that is enclosed by a sphere with the radius of the observed beam size ( $R_{\text{beam}}$ ), as illustrated in Fig 7, the total enclosed mass

$$M_{\text{beam}} = N R_c^3 \rho_c \quad (11)$$

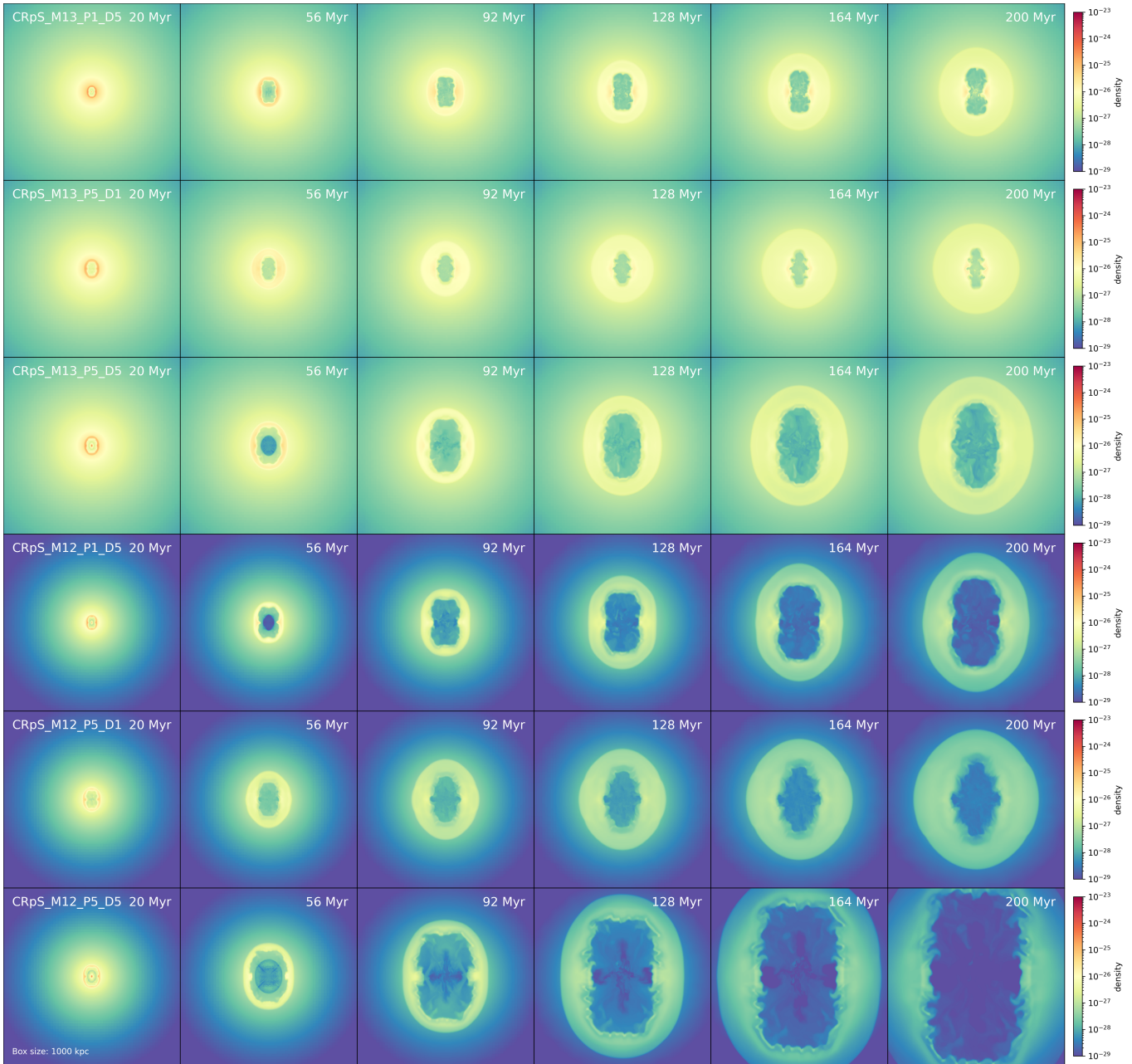


**Figure 4.** Time series of the side-on density slices of the six simulations described in Section 3.2. The top three rows show systems with virial mass  $M_{\text{vir}} = 8 \times 10^{13} M_{\odot}$ , and the bottom three rows are for cluster masses of  $M_{\text{tot}} = 8 \times 10^{12} M_{\odot}$ . For each cluster mass, the rows from top to bottom show simulations with the jet power and duration of  $(P_0, 5D_0)$ ,  $(5P_0, D_0)$ , and  $(5P_0, 5D_0)$ .

is roughly a constant with varying simulation resolution, where  $N$  is the number of clumps within the sphere,  $R_c$  is the radius of the clump, and  $\rho_c$  is the density of the clump. Therefore, the effective emissivity is the total luminosity of the clumps ( $NR_c^3\epsilon_c$ ) divided by the volume of the sphere

$$\epsilon_{\text{beam}} = \frac{NR_c^3\epsilon_c}{R_{\text{beam}}^3} \propto \frac{NR_c^3\rho_c e_{\text{cr}} B^2}{R_{\text{beam}}^3} \propto e_{\text{cr}} B^2. \quad (12)$$

With increasing simulation resolution, the clumps would be better resolved (with reduced  $R_c$ ), and  $e_{\text{cr}}$  and  $B$  would both be enhanced in the clumps due to the compression. It is therefore hard to predict the exact brightness of the simulated ORCs. The assumed magnetic field strength also has a great impact on the synchrotron emissivity ( $\epsilon_{\text{sync}} \propto B^2$ ). While the plasma  $\beta$  is observationally constrained to approximately 100 in galaxy clusters, there exists no definitive constraint on the mag-

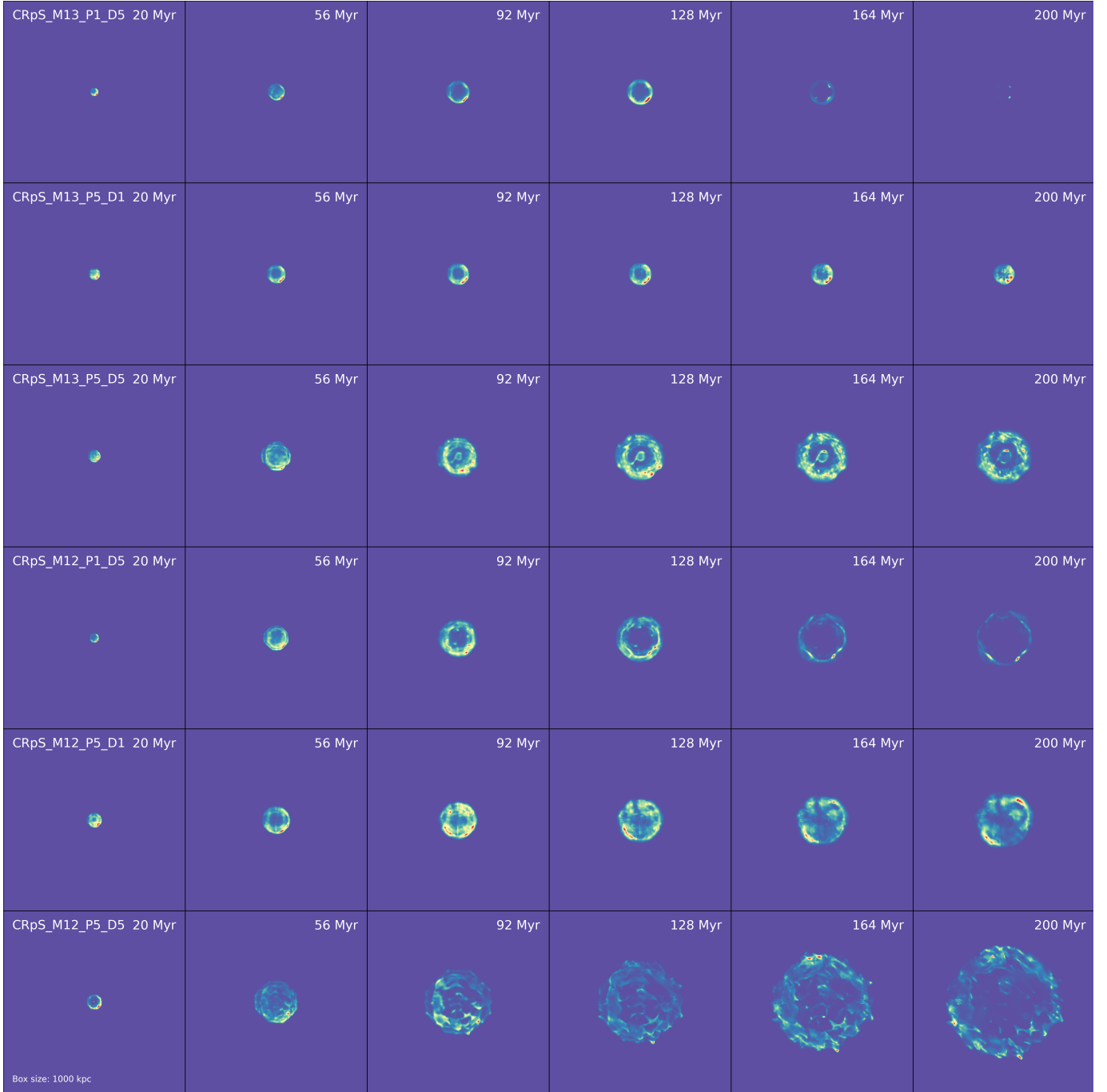


**Figure 5.** Time series of the radio morphology of the six simulations described in Section 3.2. The order of each panel is the same as in Fig. 4. Note that the surface brightness in each image is normalized by its maximum value in order to emphasize the morphology. In reality, synchrotron emission from earlier snapshots are generally much brighter than the later ones since the CR energy density decreases due to adiabatic expansion.

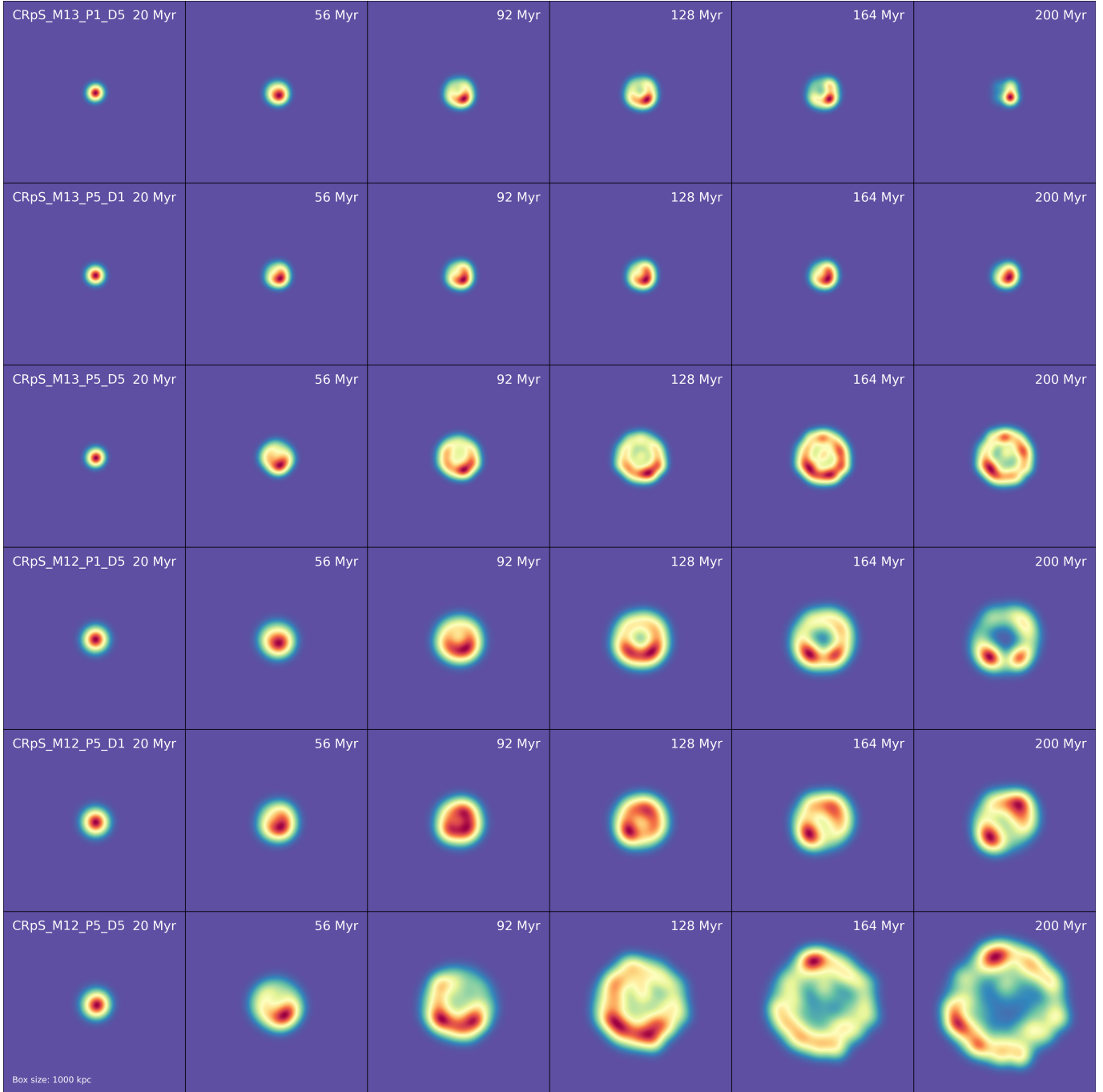


**Figure 6.** Identical to Fig. 5 but smoothed with the corresponding beam size. M13 simulations are assumed to be located at  $z = 0.27$  (i.e., the observed redshift of ORC5) and M12 simulations are assumed to be located at  $z = 0.551$  (the redshift of ORC1).

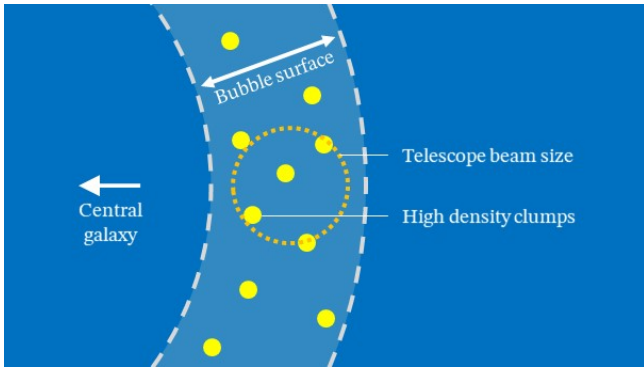


**Figure 7.** Schematic diagram of the structure of bubble surface.

netic field strength at the scale of hundreds of kpc for a group-like system. Using the self-similar scaling relations described in Section 2, the magnetic field strength for the M12 and M13 halos at the scales of a few hundreds of kpc is on the order of  $0.3 \mu\text{G}$  and  $0.06 \mu\text{G}$ <sup>1</sup>, respectively. A mere scaling of the magnetic field strength to a few  $\mu\text{G}$  could result in a remarkable increase in synchrotron emissivity by a factor of  $10^4$ . Given the lack of constraints on crucial factors on both theoretical (clump sizes) and observational (magnetic field strength) sides, we conclude that a robust prediction of the absolute luminosity should be addressed with more sophisticated simulations and is left for future investigation.<sup>2</sup>

#### 4.3. Detectability in X-ray

To further investigate the possible observable signatures of the AGN bubble scenario, we use pyXSIM (ZuHone & Hallman 2016) to predict whether our simulated ORCs can be detected by current and future X-ray observatories, namely Chandra ACIS-I, AXIS (Reynolds et al. 2023), and the Wide Field Instrument (WFI) on Athena.<sup>3</sup> Details regarding the mock observations can be found in Section A.

As shown in Fig. 8, the CRpS\_M13\_P5\_D5 case manifests a prominent thick X-ray ring. The inner edge of the ring corresponds to the high-density and turbulent bubble surface, while the outer boundary represents the shock front. We find that a long exposure time ( $\sim 1$  Ms) is required for robust detection using Chandra. Conversely, AXIS and Athena could

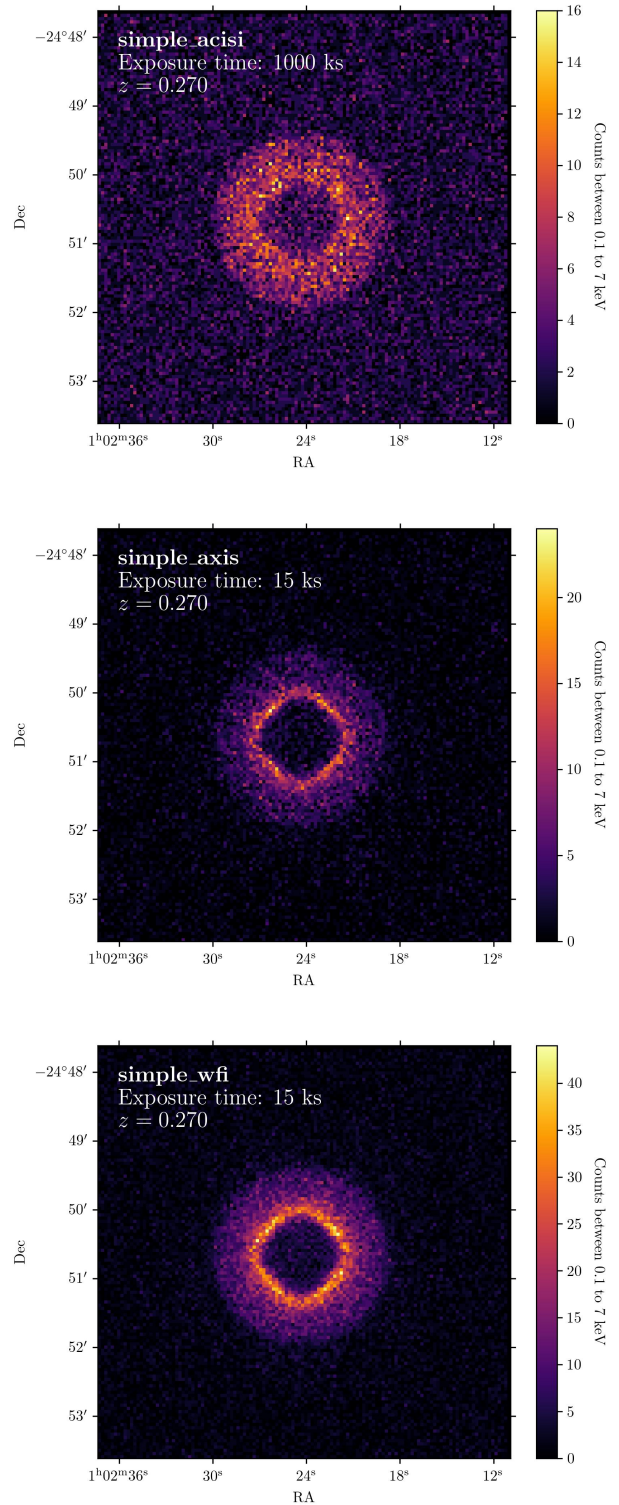


**Figure 8.** Mock X-ray observation of the CRpS\_M13\_P5\_D5 simulation using pyXSIM. The field of view of each image is  $6' \times 6'$ . For better visualization, all the images are binned to a dimension of  $128 \times 128$  regardless the actual pixel size; instrumental artifacts (such as gaps between ACIS-I CCDs) are also removed.

<sup>1</sup> This is obtained by doing an synchrotron emissivity weighted average of the magnetic field strength.

<sup>2</sup> In fact, most of the theoretical studies of the ORCs so far have not yet presented clear conclusions on the absolute brightness.

<sup>3</sup> ESA's Science Programme Committee has endorsed a rescoped version of the Athena X-ray observatory, called NewAthena, on November 8th, 2023. While the design of the mission is revised, the overall capability remains comparable.

achieve a superior signal-to-noise ratio with significantly shorter exposure times ( $\sim 15$  ks). On the other hand, mock observations of CRpS\_M12\_P5\_D5 show no detection using all three instruments up to 1 Ms of integration time. This is mainly due to the larger distance ( $z = 0.551$ ) and the lower gas density (because free-free emissivity  $\epsilon_{\text{ff}} \propto \rho^2 T^{1/2}$ ). Observationally, to date there has been no detection of X-ray counterpart of ORCs in the archival data (Norris et al. 2021a). Our results, namely, the long exposure time required for M13 and non-detection for M12, is consistent with the currently available X-ray constraints. Deep X-ray observations, especially using the upcoming X-ray telescopes, could be a powerful way to verify our model predictions.

#### 4.4. Is the energy injection reasonable?

As mentioned in Section 3.2 and 4, the jets must be powerful enough to evacuate the inner atmosphere of the ICM/IGM to produce the observed features of ORCs. Otherwise, radiative cooling would cause the ambient gas to collapse back onto the bubbles and prevent the bubbles from growing to a sufficiently large size to match with the observed ORCs. It is therefore reasonable to ask: are the assumed jet power and duration reasonable and consistent with the general picture of galaxy evolution?

While the exact power and duration (or duty cycle) of AGN jets are still poorly constrained observationally, recent theoretical advancements could provide hints for the origin of such strong and long-duration jets. Anglés-Alcázar et al. (2017) and Byrne et al. (2023) have found that, in a series of Feedback In Realistic Environments (FIRE) simulations, the growth of supermassive black holes (SMBHs) is suppressed in the early phase of galaxy evolution by efficient stellar feedback at the galaxy center. Only after the galaxy has accumulated a sufficient stellar mass or has established a virialized circumgalactic medium (CGM), would the stellar gravitational potential and CGM pressure be sufficient to trap the gas inside the galaxy and feed the central SMBH. When that happens, the SMBH would go through a phase of rapid growth (called “SMBH growth transitions” by these authors) and catch up to the observed  $M_{\text{BH}}-M_{\star}$  relation measured at low redshifts. The point of the transition is found to happen at around  $M_{\star} \sim 10^{10.5} M_{\odot}$  or  $M_{\text{halo}} \sim 10^{12} M_{\odot}$ . Interestingly, Yang et al. (2024) also found that jet-mode feedback in the SIMBA cosmological simulations tends to happen when galaxies reach  $M_{\star} \sim (1 - 5) \times 10^{10} M_{\odot}$  regardless of the redshift. In comparison, the stellar masses of ORC host galaxies (ORC1c, ORC4c, and ORC5c) are found to be around  $M_{\star} \sim 10^{11.5}$ , and their SMBH masses are around

$10^{8.7} M_{\odot}$  (Rupke et al. 2023). Though the stellar masses predicted by the simulations and the observed ones do not match exactly, it is an interesting conjecture that the ORCs might be the remnants of powerful jets launched by the accretion during the SMBH growth transition. The observed SMBH masses are also sufficient to drive the powerful jets required in our scenario with an Eddington rate of  $\sim 40\%$ . If this is the case, the number density of ORCs should be coupled with the cosmic star formation or stellar mass evolution, which could be easily verified by the large-scale radio survey of current (e.g. LOFAR, ASKAP, MeerKAT) and future (e.g. SKA) telescopes in the near future.

#### 4.5. Caveats

While our model could successfully explain many features of ORCs, several simplifications and caveats should be noted.

1. A constant isotropic CR diffusion coefficient ( $\kappa = 3 \times 10^{28} \text{ cm}^2 \text{ s}^{-1}$ ) is adopted for all the simulations presented in this study. In reality, the diffusion coefficient should be a function of CR energy, characteristic scale of magnetic field entanglement, turbulent velocity, and Alfvén speed  $v_A = B/\sqrt{4\pi\rho}$  (see e.g. Yan & Lazarian 2008; Sharma et al. 2009; Ehlert et al. 2018; Yang et al. 2019). Nevertheless, since many of the above properties remain largely unconstrained in the systems of interest ( $M_{\text{vir}} \sim 8 \times 10^{12} - 8 \times 10^{13}$ ), we decide to stick with the original value used in Yang et al. (2019) and Lin et al. (2023) to avoid additional complications. While the CR diffusion coefficient could influence the predicted thickness of the ORCs (since it determines how far the CRs could “leak out” from the bubble interior), the predicted sizes of the ring are determined by the overall dynamics and should be insensitive to the choice of diffusion coefficient.
2. As mentioned in Section 2.1, we intentionally reduce the level of refinement at  $r > 20$  kpc in order to save computational costs. While this enables us to simulate bubbles with large radii, and the overall dynamics of the bubbles converges with varied resolution, the hydrodynamic and thermal instabilities on the bubble surface is likely resolution dependent. Although this is not a major problem given the limited resolution of current observations (e.g. 6” in Norris et al. 2022), higher-resolution simulations are needed to allow direct comparison with future radio observations.
3. Re-acceleration of CRs by shocks or turbulence is not included in our simulations. In our scenario,

the forward shock formed due to the bubble expansion into the ambient medium could accelerate CRE at radii larger than those of the bubbles, while turbulence acceleration could be important inside and near the surface of the bubbles. These CRE could potentially provide additional synchrotron emission on top of the mechanisms considered in this work.

4. In this work, a re-scaled temperature profile from the Perseus cluster is used (Section 2.2). However, not all cool-core clusters share the same temperature profile, let alone non-cool-core clusters and galaxy groups. Since we generate the cluster density profile based on temperature, any modification to the assumed temperature profile could influence the radiative cooling rate of the ICM/IGM. Consequently, such alterations could potentially impact the mass flux that falls back onto the bubbles, thereby influencing the size of the bubbles.

## 5. CONCLUSIONS

The ORCs are newly discovered extragalactic radio objects with unknown origin. In this work, we performed 3D CR-MHD simulations and demonstrated that end-on CRp dominated AGN bubbles is a plausible formation scenario for the ORCs. We find that, in order to produce the observed features (circular, large radius, and edge-brightened) of the ORCs, the AGN jets must be powerful enough to evacuate all the high density gas near the center of the halo, and hence lower-mass clusters or groups are more likely to host the ORCs. For successful cases, the high hadronic collision rates on the bubble surface could produce secondary particles that emit synchrotron radiation, forming limb-brightened radio morphology. The radio morphology remains consistent with ORC1 with viewing angles up to  $\sim 30^\circ$  with

respect to the jet axis, relieving the requirement of perfect alignment in the AGN scenario discussed in previous studies. We discussed about the possibility of detecting X-ray counterpart emission using deep or upcoming X-ray observations. We further postulate that under the AGN bubble scenario, the formation of ORCs might be connected to the SMBH growth transition found in recent cosmological simulations.

In the future, we aim to further calculate the absolute synchrotron intensity, polarization, and spectral index of the simulated radio emission, which will enable direct comparison with the results in [Norris et al. \(2022\)](#). This will provide a more comprehensive picture and a crucial test for the AGN scenario as the origin of ORCs.

## 6. ACKNOWLEDGMENTS

YHL and HYKY acknowledge support from National Science and Technology Council (NSTC) of Taiwan (MOST 109-2112-M-007-037-MY3; NSTC 112-2628-M-007-003-MY3). HYKY acknowledges support from Yushan Scholar Program of the Ministry of Education (MoE) of Taiwan. We thank Ellis Owen for providing insightful comments on radio emission generated by CRs. This work used high-performance computing facilities operated by Center for Informatics and Computation in Astronomy (CICA) at NTHU. FLASH was developed in part by the DOE NNSA- and DOE Office of Science-supported Flash Center for Computational Science at the University of Chicago and the University of Rochester. Data analysis presented in this paper was conducted with the publicly available yt visualization software ([Turk et al. 2011](#)) and astropy ([Astropy Collaboration et al. 2022](#)). We are grateful to the yt development team and community for their support. This research has made use of NASA’s Astrophysics Data Systems.

## APPENDIX

### A. PYXSIM SIMULATIONS

We use pyXSIM ([ZuHone & Hallman 2016](#)) to make mock X-ray observations from the simulated gas distributions. We model the ICM as thermal plasma in collisional ionization equilibrium (CIE) with properties described by the APEC model ([Smith et al. 2001](#)) assuming a metallicity of  $Z = 0.3Z_\odot$ . We use the “tbabs” model with neutral hydrogen column density  $N_H = 4 \times 10^{20} \text{ cm}^{-2}$  to model the foreground Galactic absorption. M13 is placed at (R.A., Dec.) =  $(315.75^\circ, 62.00^\circ)$ ,  $z = 0.27$  and M12 is placed at (R.A., Dec.) =  $(15.60^\circ, -24.84^\circ)$ ,  $z = 0.551$ . The spectral range covers the energy range from 0.1 to 7 keV.

For the instruments, we utilize the `make_simple_instrument` function to eliminate instrumental artifacts while obtaining the key properties, such as effective area, for a specified instrument. We set the field of view (FOV) and image dimensions to be  $6' \times 6'$  and  $128 \times 128$ , respectively. For simplicity, we disabled dithering (`no_dither=True`) but keep the instrumental background (`no_bkgnd=False`). The instrument response files we used are:

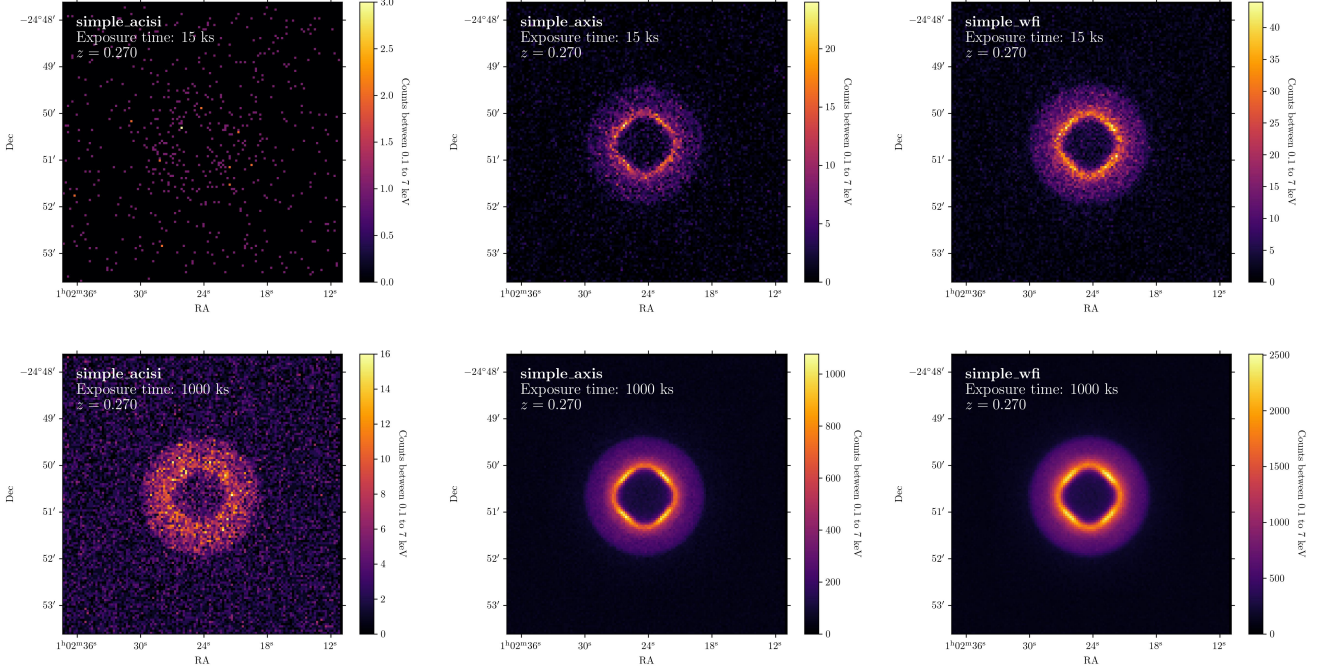


**Figure 9.** Mock X-ray images of the CRpS\_M13\_P5\_D5 simulation using pyXSIM, assuming exposure times of 15 ks (top row) and 1 Ms (bottom row), respectively. Images from left to right are obtained using Chandra, AXIS, and Athena response files, respectively. All images are binned into a  $128 \times 128$  grid for improved visualization.

1. Chandra ACIS-I: `acisi_aimpt_cy22.rmf`, `acisi_aimpt_cy22.arf`
2. AXIS: `axis_ccd_20221101.rmf`, `axis_onaxis_20221116.arf`
3. Athena WFI: `athena_wfi_sixte_v20150504.rmf`, `athena_sixte_wfi_wo_filter_v20190122.arf`

In Fig. 9, we present mock X-ray images obtained with ACIS-I, AXIS, and WFI, considering integration times of 15 ks and 1 Ms. As discussed in Section 4.3, detecting M13 poses a challenge for Chandra but is easily achievable for upcoming X-ray telescopes. Conversely, observing M12 (Fig. 10) proves to be challenging even for the next generation X-ray telescopes due to its greater distance and lower surface brightness.

## REFERENCES

- Anglés-Alcázar, D., Faucher-Giguère, C.-A., Quataert, E., et al. 2017, *MNRAS*, 472, L109, doi: [10.1093/mnrasl/slx161](https://doi.org/10.1093/mnrasl/slx161)
- Astropy Collaboration, Price-Whelan, A. M., Lim, P. L., et al. 2022, *ApJ*, 935, 167, doi: [10.3847/1538-4357/ac7c74](https://doi.org/10.3847/1538-4357/ac7c74)
- Birzan, L., McNamara, B. R., Nulsen, P. E. J., Carilli, C. L., & Wise, M. W. 2008, *ApJ*, 686, 859, doi: [10.1086/591416](https://doi.org/10.1086/591416)
- Blandford, R., Meier, D., & Readhead, A. 2019, *ARA&A*, 57, 467, doi: [10.1146/annurev-astro-081817-051948](https://doi.org/10.1146/annurev-astro-081817-051948)
- Bourne, M. A., & Yang, H.-Y. K. 2023, *Galaxies*, 11, 73, doi: [10.3390/galaxies11030073](https://doi.org/10.3390/galaxies11030073)
- Byrne, L., Faucher-Giguère, C.-A., Stern, J., et al. 2023, *MNRAS*, 520, 722, doi: [10.1093/mnras/stad171](https://doi.org/10.1093/mnras/stad171)
- Carilli, C. L., & Taylor, G. B. 2002, *ARA&A*, 40, 319, doi: [10.1146/annurev.astro.40.060401.093852](https://doi.org/10.1146/annurev.astro.40.060401.093852)
- Coil, A. L., Perrotta, S., Rupke, D. S. N., et al. 2023, arXiv e-prints, arXiv:2310.15162, doi: [10.48550/arXiv.2310.15162](https://doi.org/10.48550/arXiv.2310.15162)
- Croston, J. H., Ineson, J., & Hardcastle, M. J. 2018, *MNRAS*, 476, 1614, doi: [10.1093/mnras/sty274](https://doi.org/10.1093/mnras/sty274)
- Dolag, K., Böss, L. M., Koribalski, B. S., Steinwandel, U. P., & Valentini, M. 2023, *ApJ*, 945, 74, doi: [10.3847/1538-4357/acb5f5](https://doi.org/10.3847/1538-4357/acb5f5)
- Dunn, R. J. H., & Fabian, A. C. 2004, *MNRAS*, 355, 862, doi: [10.1111/j.1365-2966.2004.08365.x](https://doi.org/10.1111/j.1365-2966.2004.08365.x)

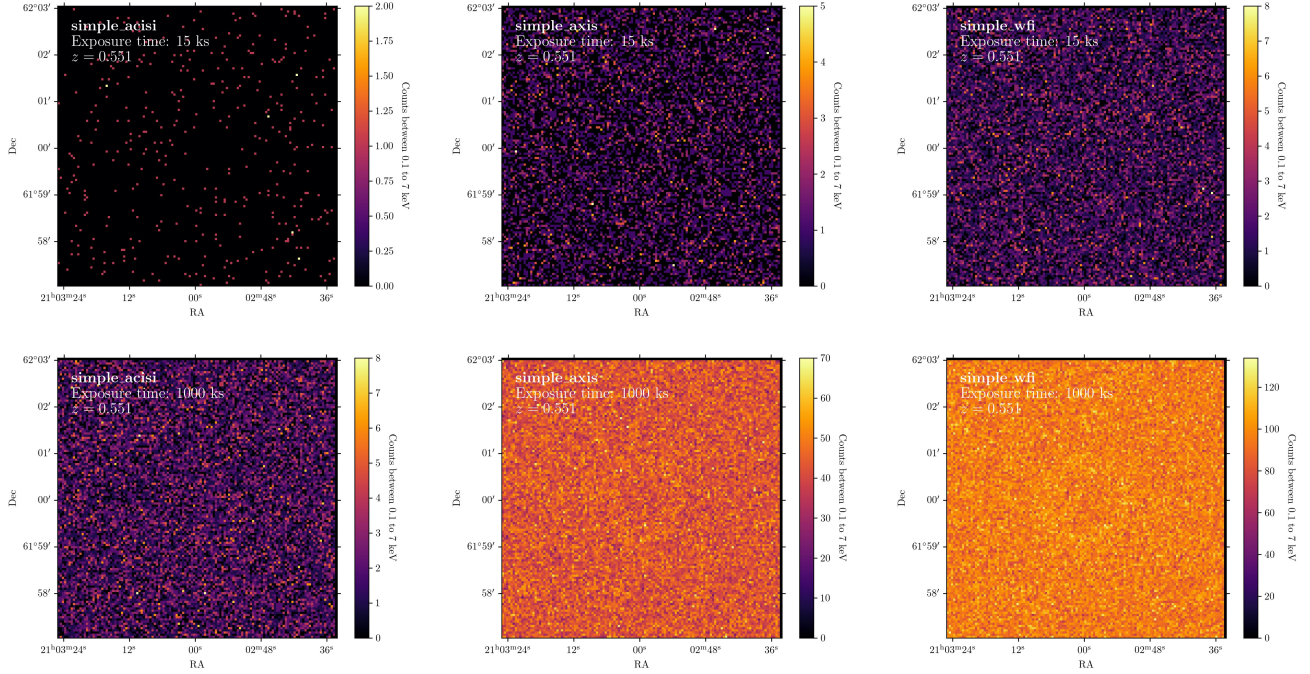


**Figure 10.** Same as Fig 9, but for the CRpS\_M12.P5.D5 simulation.

- Ehler, K., Weinberger, R., Pfrommer, C., Pakmor, R., & Springel, V. 2018, arXiv: 1806.05679.  
<https://arxiv.org/abs/1806.05679>
- Feretti, L., Giovannini, G., Govoni, F., & Murgia, M. 2012, *A&A Rv*, 20, 54, doi: [10.1007/s00159-012-0054-z](https://doi.org/10.1007/s00159-012-0054-z)
- Fryxell, B., Olson, K., Ricker, P., et al. 2000, *ApJS*, 131, 273, doi: [10.1086/317361](https://doi.org/10.1086/317361)
- Gupta, N., Huynh, M., Norris, R. P., et al. 2022, *PASA*, 39, e051, doi: [10.1017/pasa.2022.44](https://doi.org/10.1017/pasa.2022.44)
- Jonas, J., & MeerKAT Team. 2016, in *MeerKAT Science: On the Pathway to the SKA*, 1, doi: [10.22323/1.277.0001](https://doi.org/10.22323/1.277.0001)
- Kaiser, N. 1986, *MNRAS*, 222, 323
- Koribalski, B. S., Norris, R. P., Andernach, H., et al. 2021, *MNRAS*, 505, L11, doi: [10.1093/mnrasl/slab041](https://doi.org/10.1093/mnrasl/slab041)
- Koribalski, B. S., Veronica, A., Brüggem, M., et al. 2023, arXiv e-prints, arXiv:2304.11784, doi: [10.48550/arXiv.2304.11784](https://doi.org/10.48550/arXiv.2304.11784)
- Lin, Y.-H., Yang, H. Y. K., & Owen, E. R. 2023, *MNRAS*, 520, 963, doi: [10.1093/mnras/stad185](https://doi.org/10.1093/mnras/stad185)
- Navarro, J. F., Frenk, C. S., & White, S. D. M. 1995, *MNRAS*, 275, 720
- Norris, R. P., Intema, H. T., Kapińska, A. D., et al. 2021a, *PASA*, 38, e003, doi: [10.1017/pasa.2020.52](https://doi.org/10.1017/pasa.2020.52)
- Norris, R. P., Marvil, J., Collier, J. D., et al. 2021b, *PASA*, 38, e046, doi: [10.1017/pasa.2021.42](https://doi.org/10.1017/pasa.2021.42)
- Norris, R. P., Collier, J. D., Crocker, R. M., et al. 2022, *MNRAS*, 513, 1300, doi: [10.1093/mnras/stac701](https://doi.org/10.1093/mnras/stac701)
- Owen, E. R., & Yang, H. Y. K. 2022, *MNRAS*, 516, 1539, doi: [10.1093/mnras/stac2289](https://doi.org/10.1093/mnras/stac2289)
- Reynolds, C. S., Kara, E. A., Mushotzky, R. F., et al. 2023, arXiv e-prints, arXiv:2311.00780, doi: [10.48550/arXiv.2311.00780](https://doi.org/10.48550/arXiv.2311.00780)
- Rupke, D., Coil, A., Whalen, K., et al. 2023, arXiv e-prints, arXiv:2312.06387, doi: [10.48550/arXiv.2312.06387](https://doi.org/10.48550/arXiv.2312.06387)
- Ruszkowski, M., Yang, H. Y. K., & Reynolds, C. S. 2017, *ApJ*, 844, 13, doi: [10.3847/1538-4357/aa79f8](https://doi.org/10.3847/1538-4357/aa79f8)
- Sarbadhicary, S. K., Thompson, T. A., Lopez, L. A., & Mathur, S. 2023, *MNRAS*, 526, 6214, doi: [10.1093/mnras/stad3108](https://doi.org/10.1093/mnras/stad3108)
- Sharma, P., Chandran, B. D. G., Quataert, E., & Parrish, I. J. 2009, *ApJ*, 699, 348, doi: [10.1088/0004-637X/699/1/348](https://doi.org/10.1088/0004-637X/699/1/348)
- Smith, R. K., Brickhouse, N. S., Liedahl, D. A., & Raymond, J. C. 2001, *ApJL*, 556, L91, doi: [10.1086/322992](https://doi.org/10.1086/322992)
- Tang, X., & Churazov, E. 2017, *MNRAS*, 468, 3516, doi: [10.1093/mnras/stx590](https://doi.org/10.1093/mnras/stx590)
- Turk, M. J., Smith, B. D., Oishi, J. S., et al. 2011, *ApJS*, 192, 9, doi: [10.1088/0067-0049/192/1/9](https://doi.org/10.1088/0067-0049/192/1/9)
- Yamasaki, S., Sarkar, K. C., & Li, Z. 2023, arXiv e-prints, arXiv:2309.17451, doi: [10.48550/arXiv.2309.17451](https://doi.org/10.48550/arXiv.2309.17451)
- Yan, H., & Lazarian, A. 2008, *ApJ*, 673, 942, doi: [10.1086/524771](https://doi.org/10.1086/524771)
- Yang, H. Y. K., Gaspari, M., & Marlow, C. 2019, *ApJ*, 871, 6, doi: [10.3847/1538-4357/aaf4bd](https://doi.org/10.3847/1538-4357/aaf4bd)

- Yang, H.-Y. K., & Reynolds, C. S. 2016, *ApJ*, 818, 181,  
doi: [10.3847/0004-637X/818/2/181](https://doi.org/10.3847/0004-637X/818/2/181)
- Yang, H.-Y. K., & Ruszkowski, M. 2017, *ApJ*, 850, 2,  
doi: [10.3847/1538-4357/aa9434](https://doi.org/10.3847/1538-4357/aa9434)
- Yang, H.-Y. K., Sutter, P. M., & Ricker, P. M. 2012,  
*MNRAS*, 427, 1614,  
doi: [10.1111/j.1365-2966.2012.22069.x](https://doi.org/10.1111/j.1365-2966.2012.22069.x)
- Yang, T., Davé, R., Cui, W., et al. 2024, *MNRAS*, 527,  
1612, doi: [10.1093/mnras/stad3223](https://doi.org/10.1093/mnras/stad3223)
- Yoast-Hull, T. M., Everett, J. E., Gallagher, III, J. S., &  
Zweibel, E. G. 2013, *ApJ*, 768, 53,  
doi: [10.1088/0004-637X/768/1/53](https://doi.org/10.1088/0004-637X/768/1/53)
- ZuHone, J. A., & Hallman, E. J. 2016, pyXSIM: Synthetic  
X-ray observations generator, Astrophysics Source Code  
Library, record ascl:1608.002. <http://ascl.net/1608.002>
- Zweibel, E. G. 2013, *Physics of Plasmas*, 20, 055501,  
doi: [10.1063/1.4807033](https://doi.org/10.1063/1.4807033)
- . 2017, *Physics of Plasmas*, 24, 055402,  
doi: [10.1063/1.4984017](https://doi.org/10.1063/1.4984017)